ACS OMEGA

http://pubs.acs.org/journal/acsodf

Article

Band gap and Morphology Engineering of Hematite Nanoflakes from an *Ex Situ* Sn Doping for Enhanced Photoelectrochemical Water Splitting

Hyo-Jin Ahn, Stepan Kment,* Alberto Naldoni, Radek Zbořil, and Patrik Schmuki*

Cite This: *ACS Omega* 2022, 7, 35109−35117

Read Online

ACCESS | Metrics & More | Article Recommendations | Supporting Information

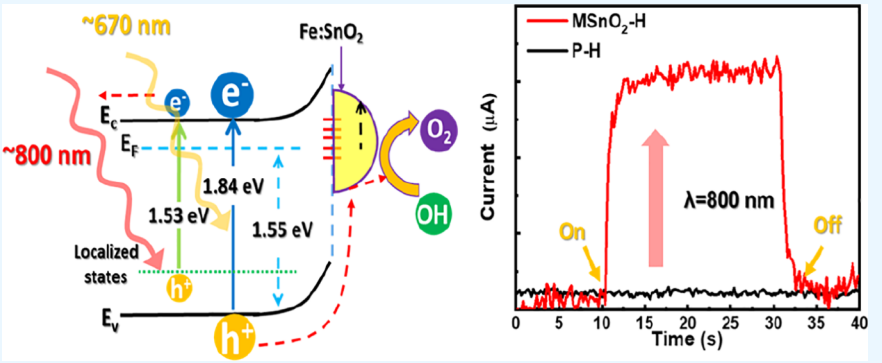

ABSTRACT: In this article, we report a simple *ex situ* Sn-doping method on hematite nanoflakes (coded as $MSnO_2$-H) that can protect the nanoflake (NF) morphology against the 800 °C high-temperature annealing process and activate the photoresponse of hematite until 800 nm wavelength excitation. $MSnO_2$-H has been fabricated by dropping $SnCl_4$ ethanol solution on hematite nanoflakes homogeneously grown over the conductive FTO glass substrate and annealed at 500 °C to synthesize the SnO_2 nanoparticles on hematite NFs. The Sn-treated samples were then placed in a furnace again, and the sintering process was conducted at 800 °C for 15 min. During this step, structure deformation of hematite occurs normally due to the grain boundary motion and oriented attachment. However, in the case of $MSnO_2$-H, the outer SnO_2 nanoparticles efficiently prevented a shape deformation and maintained the nanoflake shape owing to the encapsulation of hematite NFs. Furthermore, the interface of hematite/SnO_2 nanoparticles became the spots for a heavy Sn ion doping. We demonstrated the generation of the newly localized states, resulting in an extension of the photoresponse of hematite until 800 nm wavelength light irradiation. Furthermore, we demonstrated that SnO_2 nanoparticles can effectively act as a passivation layer, which can reduce the onset potential of hematite for water splitting redox reactions. The optimized $MSnO_2$-H nanostructures showed a 2.84 times higher photocurrent density and 300 mV reduced onset potential compared with a pristine hematite nanoflake photoanode.

INTRODUCTION

Hematite iron oxide (α-Fe_2O_3) is one of the promising candidates for the production of hydrogen via photoelectrochemical water splitting (PEC-WS) owing to its suitable band gap (2.1 eV) providing a high theoretical solar-to-hydrogen efficiency (15.3%), high chemical and photocorrosion stability, as well as earth abundance.[1−3] It is an n-type semiconductor and hence is utilized as the photoanode material in the PEC-WS cells. However, the performance of the hematite photoanodes is still limited due to several drawbacks such as a high electrical resistivity, short hole-diffusion length ($L_h \approx 2-4$ nm), high charge recombination rate, and poor oxygen evolution reaction kinetics taking place on its surface.[4−6] A number of approaches have been introduced to address these problems including, particularly, various nanostructuring and morphology controls (e.g., thin film,[7] nanoflake,[8] nanorod,[9] and nanoporous structure[10]), doping by foreign elements (Sn^{4+},[11] Ti^{4+},[12] Pt^{4+},[13] B^{3+},[14] etc.), deposition of cocatalysts on the hematite surface (e.g., Zn-Co LDH,[15] Co-Pi,[16] and FeOOH[17]), and/or deposition of isocrystalline ultrathin passivation layers.[18,19]

Morphologically controlled hematite nanostructures are highly desired in terms of increasing light absorption because of their high specific area and addressing problems associated with a short diffusion length of photoholes, which both lead to

Received: June 27, 2022
Accepted: August 31, 2022
Published: September 19, 2022

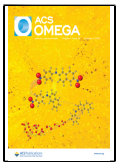

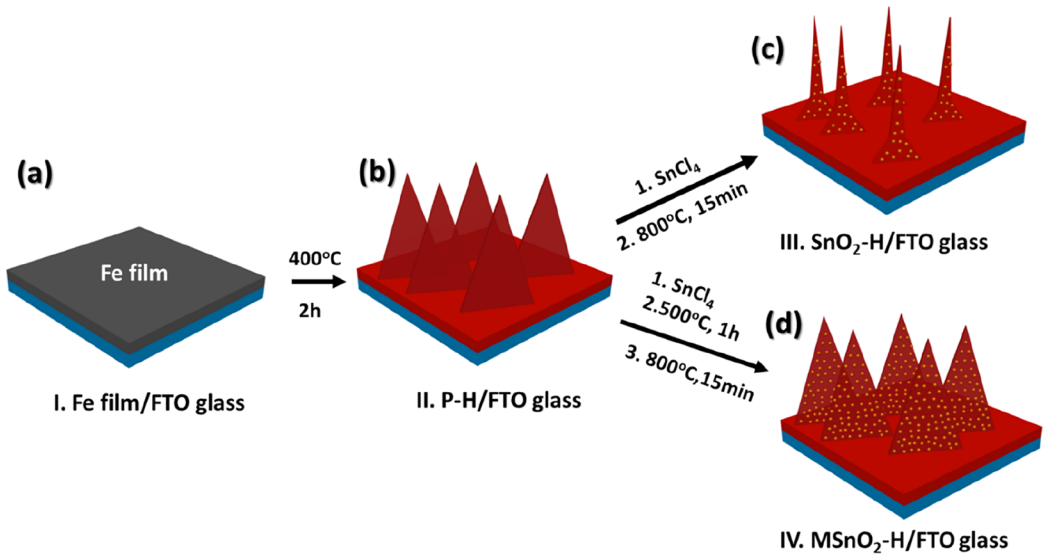

Figure 1. Schematic illustration of the fabrication procedures for (a) Fe film, (b) P-H (Fe_2O_3 NF), (c) SnO_2-H, and (d) $MSnO_2$-H, respectively.

a significantly enhanced PEC-WS activity.[20−22] Elemental doping is the efficient way to increase a donor density in hematite and thus the electrical conductivity.[23] Tin (Sn) is the most typical example of metal impurity used for the hematite doping. The substitution of iron by Sn^{4+} ions in the hematite lattice has led to an increase in the donor density N_D from 7.86 × 10^{19} to 1.95 × 10^{20} cm^{-3}.[24] Consequently, the dynamics of photocharges is enhanced because of better electrical conductivity. Both *in situ* and *ex situ* methods have been described to incorporate tin ions into hematite structures. In the case of *in situ* doping, Sn dopants were added to the precursor solution of hematite during hydrothermal growth.[25] *In situ* doping is a plain process that provides flexibility in the selection of dopants and uses relatively low sintering temperatures without additional doping steps.[26] However, deformation of morphology and changes in crystallinity are observed from *in situ*-doped hematite.[23] The most frequent strategy for *ex situ* doping is a thermal diffusion of tin ions coming from the FTO glass substrate (the glass substrate is coated by a conductive film of fluorine-doped SnO_2) at high temperatures (∼800 °C).[15] Correspondingly, one can use a tin-containing precursor solution deposited on the hematite or akaganeites (β-FeOOH) surface, which is then thermally treated under similar temperatures.[27] The key advantage of the *ex situ* processes is that various hematite and/or akaganeite nanostructures (nanorods,[28] nanotubes,[29] nanoflakes,[30] etc.) can be utilized as the starting substrates. Furthermore, Sn doping also leads to a slightly reduced optical band gap and enhanced optical adsorption coefficient by structural distortion of the hematite lattice.[31] In addition, from computational approaches a band gap reduction of hematite is expected by newly localized energy levels, resulting from orbital hybridization between Fe ions (3d orbital) and Sn ions (5s and 5p orbitals).[32] However, there are only a few studies dealing with the relationship between PEC performance and increased optical property of hematite.[31,33] Especially, the photoresponse at long wavelength ($\lambda \geq 650$ nm) of the incident light without plasmon resonances by novel metals and/or light-trapping structures, which is an important issue for improving the PEC performance of hematite, has been rarely reported.[34,35]

The passivation overlayers, for example, TiO_2,[18] Al_2O_3,[19] or Ga_2O_3[36] conformally and homogeneously covering the hematite surface generally provide two beneficial effects; namely, they improve stability of photoanodes by preventing a direct contact between electrolyte and hematite, as well as they passivate the detrimental surface states that work as recombination centeres. As a consequence of the surface state inactivation and thus of reduced recombination of the charge carriers, the photocurrent density increases, and simultaneously, the onset potential is shifted to a more cathodic region, which results in significantly higher PEC-WS activity.[37]

In this work, we report morphology-controlled hematite nanoflakes that were treated with a SnO_2 coating, which acts as a passivation layer ($MSnO_2$-H) and provides photoresponses at long wavelength (∼800 nm) using *ex situ* surface treatments and a high-temperature annealing process. The photocurrent density of the $MSnO_2$-H obtained is 0.847 mA/cm^2 at 1.23 V_{RHE}, which is about 16-fold enhanced PEC activity over pristine hematite nanoflakes (P-H). We attribute the significant enhancement not only to a reduced recombination by surface passivation effects that can be defined using an intensity-modulated photocurrent spectroscopy (IMPS) analysis but also to an enhanced conductivity and extended photoresponses ($650 \leq \lambda \leq 800$ nm) by newly localized energy levels resulting from a high concentration of Sn^{4+} doping.

RESULTS AND DISCUSSION

The fabrication of hematite nanoflake-based photoanodes follows several steps, as depicted in Figure 1. First, a 600 nm thick film of pure iron was deposited onto a FTO substrate by using magnetron sputtering. It is worth noting that it is a novel strategy for preparing fully transparent hematite photoanodes with a nanoflake coverage, that is, we use a total thermal oxidation of the iron thin film to obtain this morphology.[38] In the second step, the FTO/iron film substrates were annealed at 400 °C for 2 h to grow pristine hematite nanoflakes (hereafter, the samples denoted as P-H). In the third step, a precursor solution of $SnCl_4$ diluted in ethanol was drop-casted over the P-H samples and then annealed at 800 °C for 15 min (hereafter, the samples are denoted as SnO_2-H). Alternatively, prior to the high-temperature treatment, the samples were

https://doi.org/10.1021/acsomega.2c04028
ACS Omega 2022, 7, 35109−35117

annealed first at 500 °C for 1 h in order to preserve the nanoflake morphology (hereafter, the samples are denoted as $MSnO_2$-H). In other words, during the 500 °C annealing process, the thin and small SnO_2 NPs are uniformly formed on the surface of hematite nanoflakes, which can prevent a morphology deformation resulting from the restricted grain boundary motion and oriented attachment.[20] It is a strategy similar to the SiO_2 encapsulation described by Sivula et al.[39]

The top-view scanning electron microscopy (SEM) images of the hematite photoanodes treated under different conditions are displayed in Figure 2. The as-grown hematite samples

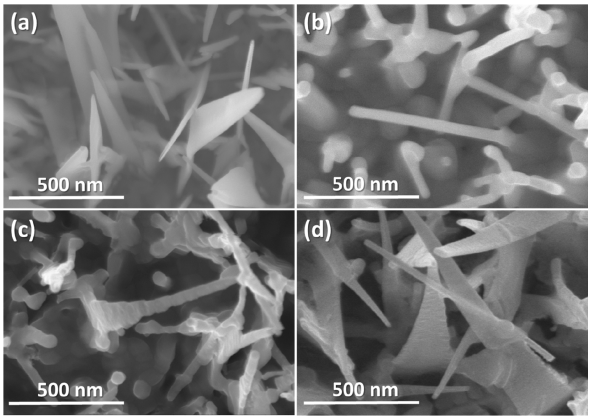

Figure 2. SEM images of (a) P-H, (b) Sn-H, (c) SnO_2-H, and (d) $MSnO_2$-H, respectively.

(Figures 2a, S1b) show a dense array of well-developed nanoflakes, having a length varying between 0.3 and 2 μm and thickness between ∼150 and ∼20 nm at the bottom and their terminating tips, respectively. During the single annealing process at 800 °C of bare hematite nanoflakes (i.e., those without applied $SnCl_4$ solution), an undesirable sintering process of the nanoflakes clearly occurred. It means that the nanoflake morphology transformed to a much sharper nanowire-like shape due to grain boundary diffusion, as demonstrated by SEM and transmission electron microscopy (TEM) images (Figures 2b and S2). In this procedure, the tin doping in the hematite lattice took place via the mechanism of the thermal diffusion of Sn^{4+} ions realized from the bottom FTO substrate (the sample is hereafter coded as Sn-H).[15,25] A semi-preserved nanoflake structure was achieved despite the same high-temperature annealing in the case of $SnCl_4$-treated hematite nanoflakes (Figure 2c). Finally, it can be observed in Figure 2d that the samples treated with the $SnCl_4$ solution and then annealed in two sequential steps, first at 500 °C for 1 h and then at 800 °C for 15 min (see Figure 1), well-maintained the desired nanoflake morphology ($MSnO_2$-H, Figure S3). During the first annealing step, the dried drops of the $SnCl_4$ precursor oxidized to SnO_2 NPs, which uniformly covered the hematite nanoflake surface. These nanoparticles then provide two functions during the following second annealing step; namely, they form an encapsulation scaffold to prevent morphology change (a simpler approach than previously reported silica encapsulation) and are a simultaneous source of the *ex situ* Sn^{4+} doping of hematite.

The TEM images of P-H, SnO_2-H, and $MSnO_2$-H are well consistent with corresponding SEM images, as shown in Figure 2. The energy-dispersive spectroscopy (EDS) mapping (Figure 3e−g) visualizes the distribution of Sn, Fe, and O ions in $MSnO_2$-H. In particular, the quantitative analysis of a single SnO_2 nanoparticle on Fe_2O_3 NF, which is calculated from EDS mapping (Figure S4), demonstrates that Sn ions from SnO_2 and Fe ions from Fe_2O_3 NF can be interchangeably diffused into each other during high-temperature annealing, leading to the formation of Fe-doped SnO_2 (F/SnO_2) and Sn-doped Fe_2O_3 in $MSnO_2$-H. As shown in Figure 3h, the particle size distribution of Fe/SnO_2 is from 1.0 to 8.1 nm with a lattice spacing of 0.33 nm, which corresponds to the (110) plane of tetragonal SnO_2 (inset of Figure 3h).[40]

The crystalline structure of the photoanodes was determined by X-ray diffraction. All the samples tested showed a well-crystalline hematite structure with the preferential orientation of the crystallites along the (110) crystalline plane, which provides the highest electrical conductivity. One of the important features is that only the P-H sample contained a contribution of the magnetite iron oxide (Fe_3O_4) phase, which commonly accompanies iron oxide nanoflakes prepared by thermal oxidation of iron substrates. The presence of magnetite, however, decreases the overall efficiency of the hematite photoanodes. Thanks to the second annealing step at 800 °C, the magnetite phase was fully transformed into the pure hematite phase.

To study the chemical compositions of the P-H and $MSnO_2$-H samples, X-ray photoelectron spectroscopy (XPS) was performed (Figures 3i and S4). Figure 3i presents the Fe 2p scans showing the Fe $2P_{3/2}$ (711 eV) and the Fe $2P_{1/2}$ (724.5 eV) peaks that are well consistent with those reported for hematite. Furthermore, the coexistence of Fe 2P peaks and an additional peak at 715.8 eV, which is indicative of the Sn $3P_{3/2}$ in $MSnO_2$-H, demonstrates the decoration of SnO_2 particles on hematite nanoflakes. In addition, the Fe ion diffusion from hematite NFs into SnO_2 (Fe/SnO_2) because of the ion diffusion due to the high-temperature sintering process can be observed by EDX mapping (Figure S4d).[15,41] The XPS analysis of the $MSnO_2$-H shows two major peaks at 487.3 eV (Sn $3d_{5/2}$) and 495.7 eV (Sn $3d_{3/2}$), which are matched with the reported XPS data for Sn-treated hematite, indicating substitutional doping of Sn^{4+} ions in the hematite lattice (Figure S5).[23] Figure S6 shows the valence band maximum (VBM) of P-H (1.20 eV) and $MSnO_2$-H (1.55 eV) assessed by linearly fitting the leading edge of the valence band retrieved from the XPS measurements. The analysis indicates that the Fermi level of $MSnO_2$-H is shifted toward the conduction band (CB) compared with pristine P-H. This Fermi-level shifting demonstrates that hematite nanoflakes are doped by Sn^{4+} ions. A concentration of 12.08% of Sn on $MSnO_2$-H was estimated from the XPS analysis. This value includes the Sn-ion doping in Fe/SnO_2 NPs. To calculate the Sn concentration of $MSnO_2$-H more precisely, we can assume that the spots of the highest Sn concentration in EDS (red spots in Figure S7) correspond to a Sn concentration of pristine SnO_2 (33.73 at. %[42]). This leads to a Sn concentration at the interface of Fe/SnO_2/hematite NFs of approximately 10−12.5% and the average Sn concentration of hematite NFs in $MSnO_2$-H of 7.5%, respectively. The band gap for the samples can be determined from the plot $(i_{ph}h\nu)^{1/2}$ *versus* photo energy ($h\nu$), where i_{ph} is photocurrent density, as shown in Figure 3k. In particular, the band gap of P-H and $MSnO_2$-H can be read as approximately 2.0 and 1.87 eV, respectively, which are the values well corresponding to those reported for hematite iron oxide. Interestingly, from the plot corresponding to the $MSnO_2$-H sample, potentially, one more value of a band gap

https://doi.org/10.1021/acsomega.2c04028
ACS Omega 2022, 7, 35109−35117

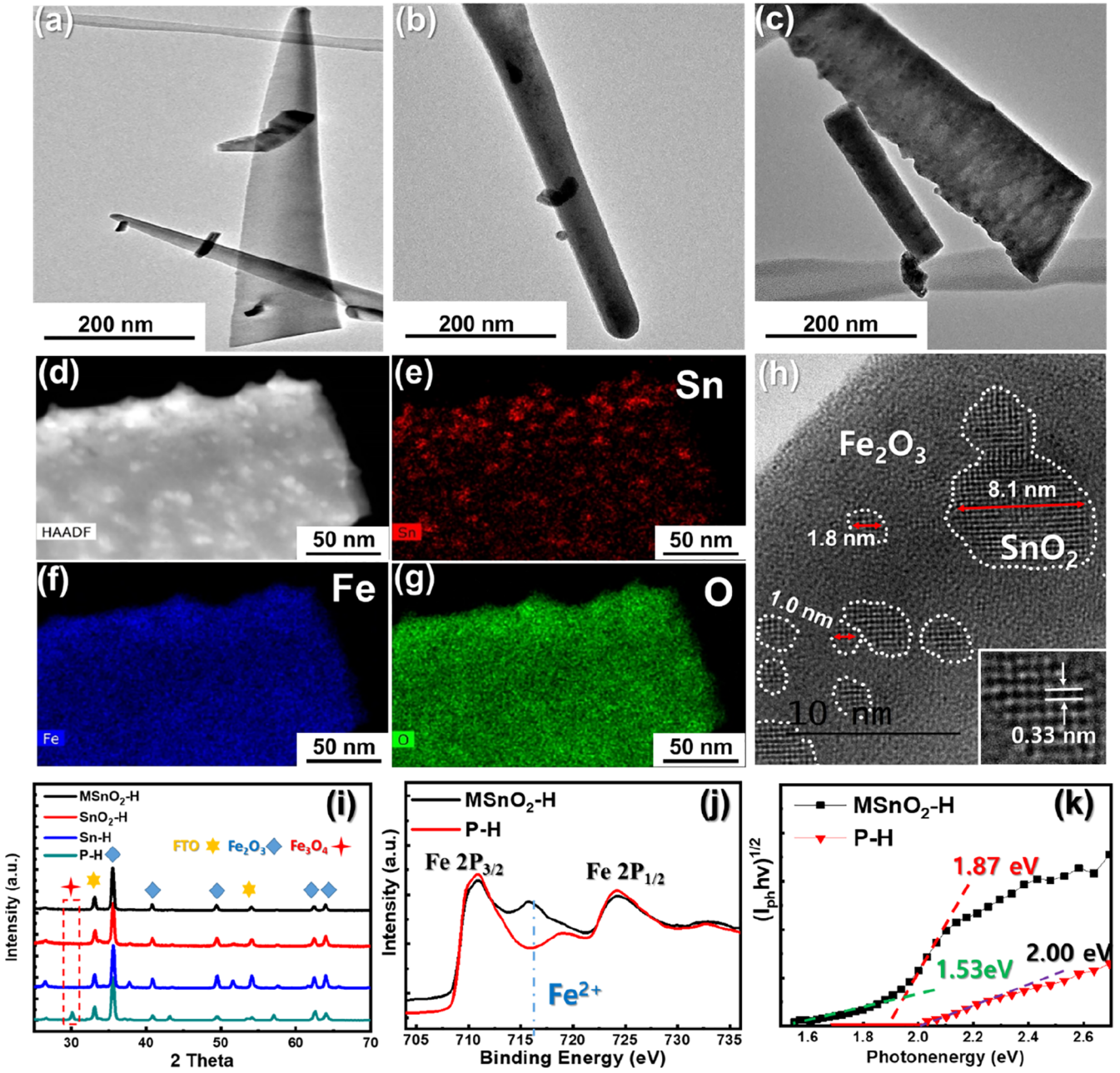

Figure 3. TEM images of (a) P-H, (b) SnO_2-H, and (c,d, and h) $MSnO_2$-H. EDS mapping images of (e) Sn-K, (f) Fe-K, and (g) O-K signals from a $MSnO_2$-H. (h) TEM image of Fe/SnO_2 NPs. Inset in (h): lattice constant of Fe/SnO_2 NPs. (i) XRD data of P-H, Sn-H, SnO_2-H, and $MSnO_2$-H, respectively, (j) Fe 2p scans for the P-H and $MSnO_2$-H, and (k) band gap calculation from an $(I_{ph}h\nu)^{1/2}$ *vs* photon energy ($h\nu$) plot of P-H and $MSnO_2$-H.

of 1.53 eV can be observed caused by newly localized energy levels resulting from the high concentration of Sn-ion doping (ca. 10−12.5%). This result is well consistent with the computational simulation, which shows the reduced band gap (1.57 eV) of hematite with 12.5 atom % of Sn.[32]

The linear sweep voltammetry of P-H, Sn-H, SnO_2-H, and $MSnO_2$-H in a 1 M KOH solution with the Ag/AgCl reference electrode under an AM 1.5 solar simulator is shown in Figure 4a. The PEC performance of the bilayer structure of hematite nanoflakes and thin film using an optimized process for its preparation has been already reported by our group elsewhere.[38] The charge compensations between the photoexcited electrons from hematite nanoflakes and photoexcited holes from the bottom hematite film layer can effectively reduce the probability of a recombination rate of photoanode. The P-H had a photocurrent density of 0.38 mA/cm^2 at 1.50 V_{RHE} and an onset potential of 1.21 V_{RHE}, and the photocurrent density of Sn-H increased by 0.63 mA/cm^2 at 1.50 V_{RHE} with an onset potential of 1.13 V_{RHE}. The increased PEC performance of the Sn-H compared with P-H is caused by not only the reduced magnetite layer located between hematite nanoflakes and FTO glass that hinders the electron transfer, as shown in X-ray diffraction (XRD) data (see Figure 3i), but also the enhanced conductivity by Sn-ion doping from bottom FTO glass due to the 800 °C annealing process. When the $SnCl_4$ was treated on Fe_2O_3 NF, as shown in Figure 1, the photocurrent density of SnO_2-H reached 0.92 mA/cm^2 at 1.50 V_{RHE} with the onset potential of 0.93V_{RHE} due to surface passivation and Sn^{4+} ion

https://doi.org/10.1021/acsomega.2c04028
ACS Omega 2022, 7, 35109−35117

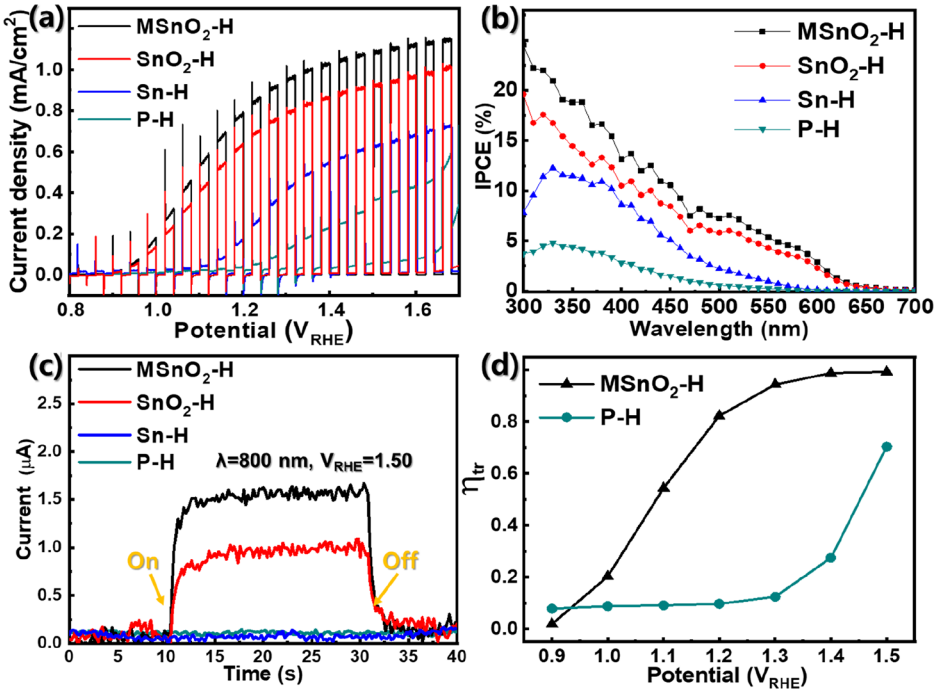

Figure 4. (a) Linear sweep voltammetry for P-H, Sn-H, SnO_2-H, and $MSnO_2$-H with chopped light under 1 sun condition. (b) IPCE of P-H, Sn-H, SnO_2-H, and $MSnO_2$-H measured at 1.50 V_{RHE}. (c) Chronoamperometry measurements of P-H, Sn-H, SnO_2-H, and $MSnO_2$-H at 1.50 V_{RHE} under illumination (λ = 800 nm). (d) Charge transfer efficiency of P-H and $MSnO_2$-H calculated from the IMPS measurement.

doping. In addition, the photocurrent density of $MSnO_2$-H is further enhanced to 1.08 mA/cm^2 at 1.50 V_{RHE} with an onset potential of 0.93 V_{RHE}. This can be ascribed to the larger surface area of $MSnO_2$-H than that of SnO_2-H obtained by a simple morphology engineering, which helps to preserve the shape of nanoflakes similar to P-H compared with SnO_2-H (nanowire-like shape, Figure 3b). As a consequence, more light, including long wavelength, can be absorbed by the nanoflakes, and thus a higher photocurrent density can be reached. The IPCE data in Figure 4b shows a higher photoresponse of $SnCl_4$-treated samples compared to that of P-H and Sn-H according to the wavelength at 1.50 V_{RHE}. Although the IPCE values of P-H from 500 to 650 nm wavelength could not be detected, the IPCE values of SnO_2-H and $MSnO_2$-H can clearly be observed from 500 to 650 nm due to decreased recombination and the electron−hole pairs (EHPs), which are generated by newly localized states due to a high concentration of Sn doping. To compare the photoresponse of samples at 800 nm wavelength, the chronoamperometry was measured in a 1 M of KOH electrolyte and at an applied bias of 1.50 V_{RHE} under chopped light illumination. The acquired data are presented in Figure 4c. The photocurrent of the $MSnO_2$-H is found to be 1.5 μA, whereas that of Sn-H and P-H is approximately zero. The higher photocurrent of $MSnO_2$-H than SnO_2-H may be attributed to the higher amount of absorbers resulting from a wider hematite nanoflake because of the morphology-controlled process, as shown in Figures 2 and 3.

To further clarify the photoresponses of P-H and $MSnO_2$-H, the photocurrent was measured at the applied potential bias of 1.50 V_{RHE} and particularly under different wavelengths of light illuminating the samples. The results are shown in Figure S8a,b. Although the photoresponse of P-H was negligible for the incident wavelengths higher than 620 nm, which is consistent with its band gap energy (2.0 eV) of hematite, the photoresponse of $MSnO_2$-H extended to the wavelength of 800 nm. As reported elsewhere, the localized Fe^{2+} 3d derived states are generated above the top of the valence band (VB) of hematite when the extra electron from Sn^{4+} converts a neighboring Fe^{3+} to a localized Fe^{2+}.[32,43] The Fe^{2+}-localized gap states in Sn-doped hematite have been observed by using a combination of XPS VB spectra and DFT + U calculation.[44] With increasing Sn contents in Fe_2O_3, the number of localized Fe^{2+} 3d gap states increases—this is in line with the previous literature.[44] The extended absorption of $MSnO_2$-H can be ascribed to the newly created localized Fe^{2+} 3d states caused by Sn doping between the VB and CB of hematite, which can absorb photons of smaller energy to generate photoexcited EHPs, which can participate in the PEC reaction.[32,45]

To elucidate the role of the Fe/SnO_2 NPs as a passivation layer, the charge transfer (K_t) and surface recombination (K_r) rate constants of P-H and $MSnO_2$-H are calculated by using IMPS responses, as shown in Figure S9. The calculation for P-H (Figure S9b) shows that K_r slightly decreases until 1.4 V_{RHE} and significantly decreases at 1.5 V_{RHE}, while the K_t remains constant over the entire potential. Although the K_t of $MSnO_2$-H shows a similar trend with Fe_2O_3 NF after 1.0 V_{RHE}, the K_r of the $MSnO_2$-H shows a steep negative slope from 0.9 V_{RHE}, which indicates reduced recombination, as shown in Figure S9c. Figure 4d shows the charge transfer efficiency [η_{tr}, defined as $K_t/(K_t + K_r)$], which is involved in the charge transfer reaction as a function of potential for P-H and $MSnO_2$-H.[6,46] The η_{tr} of P-H is lower than 0.2 until bias potential of 1.3 V_{RHE}, which means that most of the holes are trapped by surface states of hematite, and it is barely increased to 0.6 at a bias potential of 1.5 V_{RHE}. The η_{tr} of SnO_2-H (Figure S10) and $MSnO_2$-H is higher than that of the P-H after 1.0 V_{RHE}, which demonstrates that Fe-doped SnO_2 NPs on the surface of hematite help facile charge transfer from the space charge region to the electrolyte by effectively decreasing the

https://doi.org/10.1021/acsomega.2c04028
ACS Omega 2022, 7, 35109−35117

recombination resulting from passivated surface states of the hematite. This indicates that tiny Fe-doped SnO_2 NPs (1.0–8.1 nm) can be a superior passivation layer on hematite.

Last but not the least, to elucidate the charge transfer mechanism between the surface of the hematite and electrolyte, electrochemical impedance spectroscopy (EIS) was carried out in the frequency range of 100 kHz to 0.1 Hz at 1.50 V_{RHE} of applied bias and with 369 nm light source.[15] Nyquist plots for the P-H, Sn-H, SnO_2-H, and $MSnO_2$-H were fitted by using the equivalent circuit model shown in the inset image of Figure 5. The equivalent circuit consisted of the series

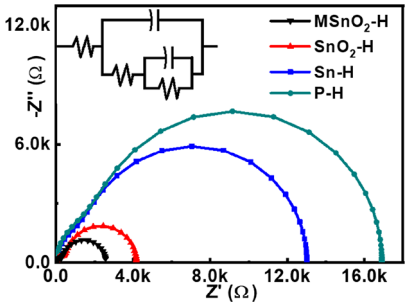

Figure 5. Nyquist plots of P-H, Sn-H, SnO_2-H, and $MSnO_2$-H under a 369 nm LED source at 1.50 V_{RHE}. The inset image is an equivalent circuit model for fitting the experimental data.

resistance of the electrochemical cell, namely R_s, the trapping/detrapping resistance of electrons, R1, the space charge capacitance of the bulk hematite, C1, the charge transfer resistance between the electrolyte and the surface of the hematite, R2, and the space charge capacitance at the interface between the electrolyte and the surface of the hematite, C2. The R_s values for every sample show similar values, indicating the same experimental condition in the electrochemical measurement.[47] Since the Sn^{4+} ions by diffusion from bottom FTO glass can effectively increase the conductivity of hematite, the R1 and R2 value of Sn-H (3,550 and 9,449 Ω) is lower than that of the P-H (4,608 and 12,380 Ω), as shown in Figure 5 and Table S2.[48] After the decoration of the SnO_2 NPs on Fe_2O_3 NF by an *ex situ* $SnCl_4$ solution treatment, the R1 and R2 value of $MSnO_2$-H is decreased to 649.3 and 3,510 Ω, respectively. This indicates that the SnO_2 NPs on hematite NF act as a passivation layer, which strongly suppresses the surface recombination owing to the reduced surface defect states, causing the high charge recombination and inefficient water oxidation by photogenerated holes.

Taking into consideration XPS, band gap calculation, photoresponse, and IMPS measurement, the band diagram of P-H and $MSnO_2$-H can be described, as illustrated in Figure 6a,b, respectively. When P-H absorbs the light, the electron–hole pairs (EHPs) are generated. Although the EHPs, which are generated in the depletion region, can be flowed to the electrolyte to participate in the water splitting reaction, the photoexcited holes in P-H are captured by surface states, resulting in recombination at the surface of P-H, as aforementioned. Meanwhile, the EHPs in the $MSnO_2$-H can be easily extracted from the electrolyte without recombination due to the passivation layer consisting of Fe/SnO_2 NPs. Furthermore, a high concentration of Sn doping can generate a localized Fe^{2+} 3d state above the VB, which can reduce the band gap, as described in Figures 3k and 6b. The Sn doping level at the interface of Fe/SnO_2 and hematite is higher than that of the plain surface of $MSnO_2$-H, as shown in EDS analysis (Figure S4b,c). Since the energy level of the localized Fe^{2+} 3d state is variable by the Sn doping amount, the interface between Fe/SnO_2 and hematite could be the site for absorbing the long wavelength (800 nm).[44] This demonstrates that *ex situ* doping by a high concentration of Sn^{4+} ions on hematite not only creates the passivation layer consisting of Fe/SnO_2 NPs but also reduces the band gap, which can generate additional EHPs at a long wavelength.

In conclusion, we explored shape-preserved hematite nanoflakes with Fe-doped SnO_2 NPs fabricated by a simple *ex situ* decoration method to produce an enhanced PEC performance. The SnO_2 NPs on hematite nanoflakes not only sustain the original shape of pristine hematite nanoflakes but also act as a passivation layer. Furthermore, $MSnO_2$-H showed greatly reduced recombination and presented a photocurrent current density of 1.08 mA/cm^2 at 1.50 V_{RHE}, with a photoresponse even at a long wavelength (800 nm). Our strategy demonstrates the simple way to reduce the EHP recombination of hematite NF and extend the capability of light absorption of hematite for the PEC reaction to the near-infrared region.

EXPERIMENTAL SECTION

Preparation of HNF and Sn-HB Samples. The iron films with a thickness of 600 nm were deposited on FTO glass by using the magnetron sputtering technique, as reported in our previous paper.[38] To grow the hematite NFs on the iron film, the prepared iron film/FTO samples were heated at 400 °C for 2 h in air using a furnace. The $SnCl_4$/ethanol solution was prepared by mixing ethanol/$SnCl_4$ = 200:1 (v/v). Then, 20 μL of the $SnCl_4$ ethanol solution was dropped on the hematite NFs/FTO and dried in air for 20 min. The dried $SnCl_4$ treated sample was annealed at 500 °C in the furnace for 1 h and then cooled down to room temperature. The sample was annealed once again at 800 °C for 15 min to prepare $MSnO_2$-H. For SnO_2-H (without the morphology control), the annealing procedure at 500 °C was skipped. In the case of Sn-H, the

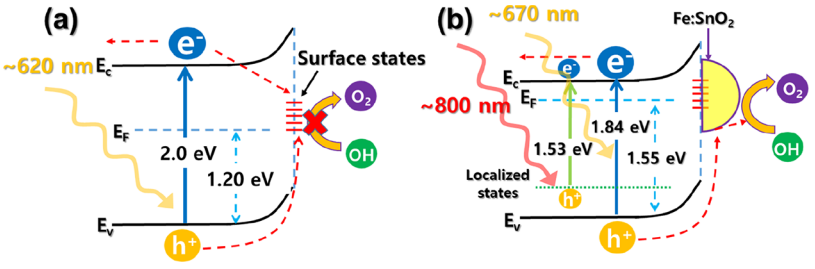

Figure 6. Schematic illustration of the energy band diagram and charge transfer process in (a) P-H and (b) $MSnO_2$-H.

https://doi.org/10.1021/acsomega.2c04028
ACS Omega 2022, 7, 35109−35117

hematite NF was placed in the furnace for 15 min at 800 °C without $SnCl_4$ treatment.

Characterization of the Samples. The morphology of the samples was investigated using SEM (Hitachi, S-4800). The EDS analysis was carried on by using a TEM machine (HRTEM, Titan G2). XRD was performed with an X'pert Philips MPD (equipped with a Panalytical X'celerator detector) with graphite monochromatic Cu Kα radiation (λ = 1.54056 Å). The chemical composition and the VBM were characterized by XPS (PHI 5600), and the peak positions were calibrated according to the C 1s peak at 284.8 eV.

Photoelectrochemical Measurements. The three-electrode system, which consists of a Pt mesh and an Ag/AgCl (3 M KCl) electrode as the counter electrode and Ag/AgCl reference electrode, respectively, was used to measure the photoelectrochemical performances of the samples under AM 1.5 illumination in 1 M KOH electrolyte. Photocurrent density was measured based on the linear sweep voltammetry method by using a potential range from −0.5 to 0.7 V at a scan rate of 2 mV s^{-1}. All potentials were converted to the reversible hydrogen electrode (RHE) using the following equation: E_{RHE} = 0.210 + $E_{Ag/AgCl}$ + 0.059 pH, where $E_{Ag/AgCl}$ is the experimentally measured potential. The incident photocurrent conversion efficiency measurements were carried out in the wavelength range from 300 to 700 nm at the fixed potential of 1.23 V_{RHE} and in the 1 M KOH electrolyte. The EIS data were obtained at 1.23 V_{RHE} in the frequency range from 100 kHz to 0.1 Hz with a 369 nm L.E.D light source. The IMPS analysis was conducted in the range from 1.0 to 1.7 V_{RHE} under 452 nm light illumination at an intensity of 10 mW/cm^2.

■ ASSOCIATED CONTENT

Supporting Information

The Supporting Information is available free of charge at https://pubs.acs.org/doi/10.1021/acsomega.2c04028.

Cross-sectional SEM image of 600 nm of iron film and Fe_2O_3 NF on FTO glass; TEM image of Sn-H; high-resolution SEM image of $MSnO_2$-H; high-magnification TEM image of $MSnO_2$-H and the corresponding EDS mapping of Sn/Fe, Sn, and Fe; XPS spectra of Sn 3d scans, O 1s scans for the P-H and $MSnO_2$-H; surface atomic composition obtained from XPS analysis for $MSnO_2$-H and P-H; VBM of P-H (1.20 eV) and $MSnO_2$-H (1.55 eV); calculated Sn ion concentration of $MSnO_2$-H from the EDS measurement; chronoamperometry measurements of P-H and $MSnO_2$-H at 1.50 V_{RHE} under different wavelengths; typical IMPS response for P-H and $MSnO_2$-H, respectively, as a function of applied potential and the rate constants of electron−hole recombination (K_r) and hole transfer (K_t) for P-H and $MSnO_2$-H, respectively, as a function of applied potential; IMPS response for SnO_2-H, as a function of applied potential, charge transfer efficiency of SnO_2-H calculated from IMPS measurement, rate constants of electron−hole recombination (K_r), and hole transfer (K_t) for P-H and $MSnO_2$-H, respectively, as a function of applied potential; EIS fitting results of P-H, Sn-H, SnO_2-H, and $MSnO_2$-H (PDF)

■ AUTHOR INFORMATION

Corresponding Authors

Stepan Kment − *Regional Centre of Advanced Technologies and Materials, Faculty of Science, Palacky University, 771 46 Olomouc, Czech Republic; Nanotechnology Centre, Centre of Energy and Environmental Technologies, VŠB−Technical University of Ostrava, 708 00 Ostrava-Poruba, Czech Republic;* orcid.org/0000-0002-6381-5093; Email: stepan.kment@upol.cz

Patrik Schmuki − *Regional Centre of Advanced Technologies and Materials, Faculty of Science, Palacky University, 771 46 Olomouc, Czech Republic; Department of Materials Science and Engineering, University of Erlangen-Nuremberg, D-91058 Erlangen, Germany;* orcid.org/0000-0002-9208-5771; Email: Patrik.Schmuki@ww.uni-erlangen.de

Authors

Hyo-Jin Ahn − *LSTME Busan Branch, 31, 46742 Busan, Republic of Korea; Regional Centre of Advanced Technologies and Materials, Faculty of Science, Palacky University, 771 46 Olomouc, Czech Republic; Department of Materials Science and Engineering, University of Erlangen-Nuremberg, D-91058 Erlangen, Germany;* orcid.org/0000-0003-4283-8592

Alberto Naldoni − *Regional Centre of Advanced Technologies and Materials, Faculty of Science, Palacky University, 771 46 Olomouc, Czech Republic; Department of Chemistry and NIS Centre, University of Turin, 10125 Torino, Italy;* orcid.org/0000-0001-5932-2125

Radek Zbořil − *Regional Centre of Advanced Technologies and Materials, Faculty of Science, Palacky University, 771 46 Olomouc, Czech Republic; Nanotechnology Centre, Centre of Energy and Environmental Technologies, VŠB−Technical University of Ostrava, 708 00 Ostrava-Poruba, Czech Republic;* orcid.org/0000-0002-3147-2196

Complete contact information is available at: https://pubs.acs.org/10.1021/acsomega.2c04028

Notes

The authors declare no competing financial interest.

■ ACKNOWLEDGMENTS

The authors would like to acknowledge the ERC, the DFG, the Erlangen DFG Cluster of Excellence EAM, project EXC 315 (Bridge), the DFG funCOS, and the Operational Programme Research, Development and Education-European Regional Development Fund, project no. CZ.02.1.01/0.0/0.0/15_003/0000416. S.K. and R.Z. acknowledge the funding from the Czech Science Foundation, project GA CR−EXPRO, 19−27454X. H.-J.A. acknowledges the National Research Foundation of Korea (NRF) grant funded by the Korean government (NRF-2021R1F1A1051912). The authors thank JeongEun Yoo for managing the samples and SEM measurement.

■ REFERENCES

(1) Sivula, K.; Le Formal, F.; Grätzel, M. Solar Water Splitting: Progress Using Hematite (α-Fe2O3) Photoelectrodes. *ChemSusChem* **2011**, *4*, 432−449.

(2) Ahn, H.-J.; Yoon, K.-Y.; Kwak, M.-J.; Lee, J.-S.; Thiyagarajan, P.; Jang, J.-H. MoSx supported Hematite with Enhanced Photoelectrochemical Performance. *J. Mater. Chem. A* **2015**, *3* (). DOI: 10.1039/c5ta06743j.

(3) Landman, A.; Dotan, H.; Shter, G. E.; Wullenkord, M.; Houaijia, A.; Maljusch, A.; Grader, G. S.; Rothschild, A. Photoelectrochemical Water Splitting in Separate Oxygen and Hydrogen Cells. *Nat. Mater.* **2017**, *16*, 646−651.
(4) Kennedy, J. H.; Frese, K. W. Photooxidation of Water at α - Fe2 O 3 Electrodes. *J. Electrochem. Soc.* **1978**, *125*, 709−714.
(5) Barroso, M.; Pendlebury, S. R.; Cowan, A. J.; Durrant, J. R. Charge carrier trapping, recombination and transfer in hematite (α-Fe2O3) water splitting photoanodes. *Chem. Sci.* **2013**, *4*, 2724−2734.
(6) Makimizu, Y.; Yoo, J.; Poornajar, M.; Nguyen, N. T.; Ahn, H.-J.; Hwang, I.; Kment, S.; Schmuki, P. Effects of low oxygen annealing on the photoelectrochemical water splitting properties of α-Fe2O3. *J. Mater. Chem. A* **2020**, *8*, 1315−1325.
(7) Kang, M. J.; Kang, Y. S. Ultrathin Insulating Under-Layer with a Hematite Thin Film for Enhanced Photoelectrochemical (PEC) Water Splitting Activity. *J. Mater. Chem. A* **2015**, *3*, 15723−15728.
(8) Wang, L.; Nguyen, N. T.; Zhang, Y.; Bi, Y.; Schmuki, P. Enhanced Solar Water Splitting by Swift Charge Separation in Au/FeOOH Sandwiched Single-Crystalline Fe2 O3 Nanoflake Photoelectrodes. *ChemSusChem* **2017**, *10*, 2720−2727.
(9) Wang, X.; Gao, W.; Zhao, Z.; Zhao, L.; Claverie, J. P.; Zhang, X.; Wang, J.; Liu, H.; Sang, Y. Efficient Photo-Electrochemical Water Splitting Based on Hematite Nanorods Doped with Phosphorus. *Appl. Catal., B* **2019**, *248*, 388−393.
(10) Ahn, H.-J.; Kwak, M.-J.; Lee, J.-S.; Yoon, K.-Y.; Jang, J.-H. Nanoporous Hematite Structures to Overcome Short Diffusion Lengths in Water Splitting. *J. Mater. Chem. A* **2014**, *2*, 19999−20003.
(11) Ling, Y.; Li, Y. Review of Sn-Doped Hematite Nanostructures for Photoelectrochemical Water Splitting. *Part. Part. Syst. Char.* **2014**, *31*, 1113−1121.
(12) Gao, S.; Wang, D.; Wang, Y.; Li, C.; Liu, Y.; Suzuki, N.; Terashima, C.; Fujishima, A.; Zhang, X. Activating Titanium Dopants in Hematite Photoanode by Rapid Thermal Annealing for Enhancing Photoelectrochemical Water Oxidation. *Electrochim. Acta* **2019**, *318*, 746−753.
(13) Kim, J. Y.; Magesh, G.; Youn, D. H.; Jang, J. W.; Kubota, J.; Domen, K.; Lee, J. S. Single-Crystalline, Wormlike Hematite Photoanodes for Efficient Solar Water Splitting. *Sci. Rep.* **2013**, *3*, 8.
(14) Ahn, H.-J.; Yoon, K.-Y.; Kwak, M.-J.; Park, J.; Jang, J.-H. Boron Doping of Metal-Doped Hematite for Reduced Surface Recombination in Water Splitting. *ACS Catal.* **2018**, *8*, 11932−11939.
(15) Ahn, H.-J.; Goswami, A.; Riboni, F.; Kment, S.; Naldoni, A.; Mohajernia, S.; Zboril, R.; Schmuki, P. Hematite Photoanode with Complex Nanoarchitecture Providing Tunable Gradient Doping and Low Onset Potential for Photoelectrochemical Water Splitting. *ChemSusChem* **2018**, *11*, 1873.
(16) Carroll, G. M.; Zhong, D. K.; Gamelin, D. R. Mechanistic insights into solar water oxidation by cobalt-phosphate-modified α-Fe2O3 photoanodes. *Energy Environ. Sci.* **2015**, *8*, 577−584.
(17) Kim, J. Y.; Youn, D. H.; Kang, K.; Lee, J. S. Highly Conformal Deposition of an Ultrathin FeOOH Layer on a Hematite Nanostructure for Efficient Solar Water Splitting. *Angew. Chem., Int. Ed.* **2016**, *55*, 10854−10858.
(18) Ahmed, M. G.; Kretschmer, I. E.; Kandiel, T. A.; Ahmed, A. Y.; Rashwan, F. A.; Bahnemann, D. W. A Facile Surface Passivation of Hematite Photoanodes with TiO2 Overlayers for Efficient Solar Water Splitting. *ACS Appl. Mater. Interfaces* **2015**, *7*, 24053−24062.
(19) Fan, Z.; Xu, Z.; Yan, S.; Zou, Z. Tuning the Ion Permeability of an Al2O3 Coating Layer on Fe2O3 Photoanodes for Improved Photoelectrochemical Water Oxidation. *J. Mater. Chem. A* **2017**, *5*, 8402−8407.
(20) Ahn, H.-J.; Yoon, K.-Y.; Kwak, M.-J.; Jang, J.-H. A Titanium-Doped SiOxPassivation Layer for Greatly Enhanced Performance of a Hematite-Based Photoelectrochemical System. *Angew. Chem., Int. Ed.* **2016**, *55*, 9922−9926.
(21) Li, M.; Yang, Y.; Ling, Y.; Qiu, W.; Wang, F.; Liu, T.; Song, Y.; Liu, X.; Fang, P.; Tong, Y.; Li, Y. Morphology and Doping Engineering of Sn-Doped Hematite Nanowire Photoanodes. *Nano Lett.* **2017**, *17*, 2490−2495.
(22) Wang, C. W.; Yang, S.; Fang, W. Q.; Liu, P.; Zhao, H.; Yang, H. G. Engineered Hematite Mesoporous Single Crystals Drive Drastic Enhancement in Solar Water Splitting. *Nano Lett.* **2016**, *16*, 427−433.
(23) Ling, Y.; Wang, G.; Wheeler, D. A.; Zhang, J. Z.; Li, Y. Sn-Doped Hematite Nanostructures for Photoelectrochemical Water Splitting. *Nano Lett.* **2011**, *11*, 2119−2125.
(24) Qin, D.-D.; Li, Y.-L.; Wang, T.; Li, Y.; Lu, X.-Q.; Gu, J.; Zhao, Y.-X.; Song, Y.-M.; Tao, C.-L. Sn-Doped Hematite Films as Photoanodes for Efficient Photoelectrochemical Water Oxidation. *J. Mater. Chem. A* **2015**, *3*, 6751−6755.
(25) Annamalai, A.; Shinde, P. S.; Jeon, T. H.; Lee, H. H.; Kim, H. G.; Choi, W.; Jang, J. S. Fabrication of superior α-Fe2O3 nanorod photoanodes through ex-situ Sn-doping for solar water splitting. *Sol. Energy Mater. Sol. Cells* **2016**, *144*, 247−255.
(26) Cai, L.; Cho, I. S.; Logar, M.; Mehta, A.; He, J.; Lee, C. H.; Rao, P. M.; Feng, Y.; Wilcox, J.; Prinz, F. B.; Zheng, X. Sol-Flame Synthesis of Cobalt-Doped TiO2 Nanowires with Enhanced Electrocatalytic Activity for Oxygen Evolution Reaction. *Phys. Chem. Chem. Phys.* **2014**, *16*, 12299−12306.
(27) Xi, L.; Chiam, S. Y.; Mak, W. F.; Tran, P. D.; Barber, J.; Loo, S. C. J.; Wong, L. H. A Novel Strategy for Surface Treatment on Hematite Photoanode for Efficient Water Oxidation. *Chem. Sci.* **2013**, *4*, 164−169.
(28) Annamalai, A.; Lee, H. H.; Choi, S. H.; Lee, S. Y.; Gracia-Espino, E.; Subramanian, A.; Park, J.; Kong, K.; Jang, J. S. Sn/Be Sequentially Co-Doped Hematite Photoanodes for Enhanced Photoelectrochemical Water Oxidation: Effect of Be2+ as Co-Dopant. *Sci. Rep.* **2016**, *6*, 23183. https://www.nature.com/articles/srep23183#supplementary-information
(29) Duan, S.-F.; Geng, Y.-Y.; Pan, X.-B.; Yao, X.-Q.; Zhao, Y.-X.; Li, X.; Tao, C.-L.; Qin, D.-D. Tubular Morphology Preservation and Doping Engineering of Sn/P-Codoped Hematite for Photoelectrochemical Water Oxidation. *Dalton Trans.* **2019**, *48*, 928−935.
(30) Wang, L.; Lee, C.-Y.; Mazare, A.; Lee, K.; Müller, J.; Spiecker, E.; Schmuki, P. Enhancing the Water Splitting Efficiency of Sn-Doped Hematite Nanoflakes by Flame Annealing. *Chem.—Eur. J.* **2013**, *20*, 77−82.
(31) Sivula, K.; Zboril, R.; Le Formal, F.; Robert, R.; Weidenkaff, A.; Tucek, J.; Frydrych, J.; Grätzel, M. Photoelectrochemical Water Splitting with Mesoporous Hematite Prepared by a Solution-Based Colloidal Approach. *J. Am. Chem. Soc.* **2010**, *132*, 7436−7444.
(32) Meng, X.; Qin, G.; Goddard, W. A.; Li, S.; Pan, H.; Wen, X.; Qin, Y.; Zuo, L. Theoretical Understanding of Enhanced Photoelectrochemical Catalytic Activity of Sn-Doped Hematite: Anisotropic Catalysis and Effects of Morin Transition and Sn Doping. *J. Phys. Chem. C* **2013**, *117*, 3779−3784.
(33) Li, J.; Cushing, S. K.; Zheng, P.; Meng, F.; Chu, D.; Wu, N. Plasmon-Induced Photonic and Energy-Transfer Enhancement of Solar Water Splitting by a Hematite Nanorod Array. *Nat. Commun.* **2013**, *4*, 2651.
(34) Kim, S. J.; Thomann, I.; Park, J.; Kang, J.-H.; Vasudev, A. P.; Brongersma, M. L. Light Trapping for Solar Fuel Generation with Mie Resonances. *Nano Lett.* **2014**, *14*, 1446−1452.
(35) Gao, H.; Liu, C.; Jeong, H. E.; Yang, P. Plasmon-Enhanced Photocatalytic Activity of Iron Oxide on Gold Nanopillars. *ACS Nano* **2012**, *6*, 234−240.
(36) Hisatomi, T.; Le Formal, F.; Cornuz, M.; Brillet, J.; Tétreault, N.; Sivula, K.; Grätzel, M. Cathodic Shift in Onset Potential of Solar Oxygen Evolution on Hematite by 13-Group Oxide Overlayers. *Energy Environ. Sci.* **2011**, *4*, 2512−2515.
(37) Liu, R.; Zheng, Z.; Spurgeon, J.; Yang, X. Enhanced Photoelectrochemical Water-Splitting Performance of Semiconductors by Surface Passivation Layers. *Energy Environ. Sci.* **2014**, *7*, 2504−2517.
(38) Ahn, H.-J.; Kment, S.; Yoo, J.; Truong Nguyen, N. T.; Naldoni, A.; Zboril, R.; Schmuki, P. Magnetite-Free Sn-Doped Hematite Nanoflake Layers for Enhanced Photoelectrochemical Water Splitting. *Chemelectrochem* **2022**, *9*, No. e202200066.

https://doi.org/10.1021/acsomega.2c04028
ACS Omega 2022, 7, 35109−35117

(39) Brillet, J.; Grätzel, M.; Sivula, K. Decoupling Feature Size and Functionality in Solution-Processed, Porous Hematite Electrodes for Solar Water Splitting. *Nano Lett.* **2010**, *10*, 4155−4160.
(40) Thirumala Rao, G.; Babu, B.; Ravikumar, R. V. S. S. N.; Shim, J.; Venkata Reddy, C. Structural and optical properties of Fe-doped SnO2quantum dots. *Mater. Res. Express* **2017**, *4*, 125021.
(41) Jiao, Z.; Wang, S.; Bian, L.; Liu, J. Stability of SnO2/Fe2O3 Multilayer Thin Film Gas Sensor. *Mater. Res. Bull.* **2000**, *35*, 741−745.
(42) Stranick, M. A.; Moskwa, A. SnO2 by XPS. *Surf. Sci. Spectra* **1993**, *2*, 50−54.
(43) Lad, R. J.; Henrich, V. E. Photoemission study of the valence-band electronic structure inFexO,Fe3O4, andα-Fe2O3single crystals. *Phys. Rev. B* **1989**, *39*, 13478−13485.
(44) Tian, C. M.; Li, W.-W.; Lin, Y. M.; Yang, Z. Z.; Wang, L.; Du, Y. G.; Xiao, H. Y.; Qiao, L.; Zhang, J. Y.; Chen, L.; Qi, D.-C.; MacManus-Driscoll, J. L.; Zhang, K. H. L. Electronic Structure, Optical Properties, and Photoelectrochemical Activity of Sn-Doped Fe2O3 Thin Films. *J. Phys. Chem. C* **2020**, *124*, 12548−12558.
(45) Zhou, Z.; Huo, P.; Guo, L.; Prezhdo, O. V. Understanding Hematite Doping with Group IV Elements: A DFT+U Study. *J. Phys. Chem. C* **2015**, *119*, 26303−26310.
(46) Peter, L. M.; Wijayantha, K. G. U.; Tahir, A. A. Kinetics of light-driven oxygen evolution at α-Fe2O3electrodes. *Faraday Discuss.* **2012**, *155*, 309−322.
(47) Bertoluzzi, L.; Bisquert, J. Equivalent Circuit of Electrons and Holes in Thin Semiconductor Films for Photoelectrochemical Water Splitting Applications. *J. Phys. Chem. Lett.* **2012**, *3*, 2517−2522.
(48) Wang, D.; Chen, Y.; Zhang, Y.; Zhang, X.; Suzuki, N.; Terashima, C. Boosting Photoelectrochemical Performance of Hematite Photoanode with TiO2 Underlayer by Extremely Rapid High Temperature Annealing. *Appl. Surf. Sci.* **2017**, *422*, 913−920.

https://doi.org/10.1021/acsomega.2c04028
ACS Omega 2022, 7, 35109−35117